



Asymmetric steady thermal blooming

JEREMIAH LANE,^{1,*}  BENJAMIN AKERS,¹ JONAH REEGER,¹ JUSTIN COOK,² AND MARTIN RICHARDSON³

¹Department of Mathematics and Statistics, Air Force Institute of Technology, Wright-Patterson AFB, Ohio 45433, USA

²Fibertek, Herndon, Virginia 20171, USA

³Laser Plasma Laboratory, CREOL, College of Optics & Photonics, University of Central Florida, Orlando, Florida 32816, USA

*jeremiah.lane@afit.edu

Received 27 January 2025; revised 2 April 2025; accepted 7 April 2025; posted 9 April 2025; published 28 April 2025

The thermal blooming of a thulium laser near $2\ \mu\text{m}$ in an enclosed chamber is considered, as in Cook *et al.* [Opt. Laser Technol. 146, 107568 (2022)]. The problem is modeled using the paraxial equation for the laser and the Navier–Stokes equations with a Boussinesq approximation for buoyancy-driven effects. These equations are solved numerically in the steady experimental configuration. The numerical procedure uses radial basis functions (RBFs) to approximate spatial derivatives and the hybrid Padé–Newton approach by Lane and Akers [Stud. Appl. Math. 10, e12740 (2024)] to solve the resulting system of nonlinear equations. Numerical simulations are compared to experimental results. The simulations explain the asymmetry of laser spots as the result of the influence of the tank’s boundary on the global convective flow. © 2025 Optica Publishing Group. All rights, including for text and data mining (TDM), Artificial Intelligence (AI) training, and similar technologies, are reserved.

<https://doi.org/10.1364/AO.557143>

1. INTRODUCTION

In this work, the steady thermal blooming of a laser beam propagating through a closed laboratory chamber is discussed. This study is a continuation of the work performed in Chapter 5 of the first author’s Ph.D. thesis [1]. Thermal blooming is the process, wherein a laser heats the propagation medium, causing temperature-based changes in the refractive index in the beam path [2,3]. This thermal lensing reduces the beam performance. Adaptive optics countermeasures can result in phase compensation instability (PCI) [4–6], where adaptive phase corrections at the aperture can reinforce intensity aberrations in the target plane.

Numerical simulation of thermal blooming requires knowledge of the light field, the temperature distribution, and the fluid velocity. Historical studies prescribe the fluid velocity (either as a fixed wind or a statistical description) [7–12]. Recently, the time-dependent nonlinear velocity field has been simulated directly including natural convection, from quiescent initial data [13,14]. Steady thermal blooming with natural convection has also been simulated [15,16]. Experimental studies in thermal blooming have considered beam propagation across a wide range of laser–fluid parameters such as beam power, beam wavelength, fluid medium, degree of turbulence, degree of crosswind, and propagation distance [17–20]. While many of these studies are oriented toward understanding beam propagation through the atmosphere, there is a scant discussion of the possible impact that the finite experimental domain may have on the beam wavefront via the laser–fluid interaction, especially in the steady-state regime. In this work, the steady-state thermal

blooming of a Gaussian laser with wavelength near $\lambda \approx 2\ \mu\text{m}$ within a climate controlled, 5.3 m long chamber is simulated and compared to the experiment. The simulations result in asymmetric crescent-shaped beam spots, providing an explanation for the observed asymmetries in the experiment. The influence of the experimental domain on the fluid dynamics of beam propagation is novel to the thermal blooming literature, with natural implications on experimental design for thermal blooming studies.

Both simulation and experimentation come with unique challenges when attempting to account for the fully coupled physical processes involved in laser propagation through an absorbing fluid. The steady fluid dynamics in response to the absorption of the beam are often dominated by natural convection, yet historical simulations for laser propagation have relied on a prescription of the fluid velocity via scaling laws or enforced crosswind [2,3,21]. To fully model the convective flow dynamics within a prescribed domain, it is beneficial to directly simulate the flow response to the laser in a buoyancy-driven framework. A difficult limitation presented in the steady-state simulation [15,16] is the reduction of computable laser-forcing amplitudes of the fixed-point fluid solver as a function of increased domain size. Recent work by the authors, however, offers a composite Padé–Newton method to compute steady-flow solutions for arbitrarily large laser forcing and domain size [22].

The goal of this article is two-pronged with contributions in the simulation of the steady-state thermal blooming and the presentation of experimental results that describe new physical

phenomena. We investigate the steady-state thermal blooming of a Gaussian laser tuned to a water absorption wavelength within a climate controlled 5.3 m long chamber. The specific tuning of the laser wavelength allows for significant absorption of the laser into the surrounding fluid [23–25], a strategy which can be used to represent high-power lasers through an atmospheric transmission window. We present evidence to suggest that if the beam propagates horizontally off-center within the fluid domain, then the bloomed irradiance in the target plane will be skewed in the direction of the nearest wall. In an effort to simulate this phenomenon, we introduce a fully coupled steady-state simulation for thermal blooming that builds off of recent work by the authors to permit simulation for significant laser absorption over the full size of the experimental propagation chamber. We show that, due to the horizontally transverse displacement of the beam center along the propagation path, the temperature fluctuations in the chamber will induce asymmetric blooming in the horizontal direction.

The rest of the article is organized as follows. Section 2 details the experimental setup and Section 3 details the formulation of the steady-state simulations. Section 4 is dedicated to the comparison of simulated and experimental results. We observe asymmetries in the bloomed irradiance profiles and present the fluid response to the tilted beam propagation. Section 5 summarizes the article and offers key takeaways for future experimental work in laser propagation.

2. EXPERIMENTAL SETUP

The experimental setup depicting the propagation chamber is provided in Fig. 1. The fiber laser architecture leading to the aperture is the same as used in the experiments in Ref. [23]. The laser wavelength λ is tunable between 1.92 and 2.01 μm with a maximum average power of 80 W in continuous-wave operation. In the following experiments, the variable power laser is a Gaussian beam with a radius of 2.25 mm and a fixed wavelength of 1944.867 nm to correspond to a water absorption band. After

passing through the aperture, the beam enters the atmosphere-controlled propagation chamber with initially quiescent flow. The chamber is filled with air at atmospheric pressure, with the same conditions as the thermal blooming experiments in Ref. [23]. The relative humidity was 50% and the fluid temperature was 296 K. The beam reflects off of a movable ceramic backstop, and the resultant irradiance profile is imaged with an FLIR camera through windows along the side of the chamber.

In an attempt to remove optical backscatter, the beam is initially reflected twice such that the resulting path traveling through the chamber is tilted in the transverse, horizontal direction. Figure 2 shows a top-down view of the propagation chamber, depicting the initial reflections and the subsequent horizontal tilting of the beam. Figure 3 provides a detailed description of the (not to scale) geometry of the mirror arrangements within the chamber.

The tilting angle θ is determined *a posteriori* via the horizontal separation of the beam spot between two propagation distances. We observe a horizontal shift in the beam spot of 1 cm for every 1 m of longitudinal propagation, so the effective tilting angle is $\theta \approx 0.01$ rad; small enough to maintain the validity of the paraxial model for beam evolution. The beam reflects off of the second mirror at a location of $x_0 = -8.9$ cm relative to the transverse center of the domain and reflects off of the ceramic backstop at a location of $x_f = -4.9$ cm for 5 m of propagation. The beam is centered vertically throughout the propagation chamber, with vertical variations in intensity due exclusively to thermal blooming. The FLIR camera captures the time dynamic laser irradiance with a frequency of 100 Hz and a frame integration time of 928 μs .

3. NUMERICAL METHODS

A. Governing Models

The paraxial equation is used as a model for the laser propagation [26]. With the same order of accuracy as the paraxial scaling for the evolution of the laser, the fluid flow is two-dimensional

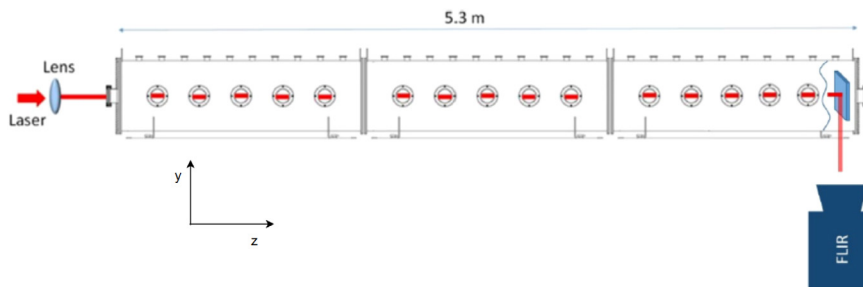


Fig. 1. Side view of the propagation chamber with coordinate axes.

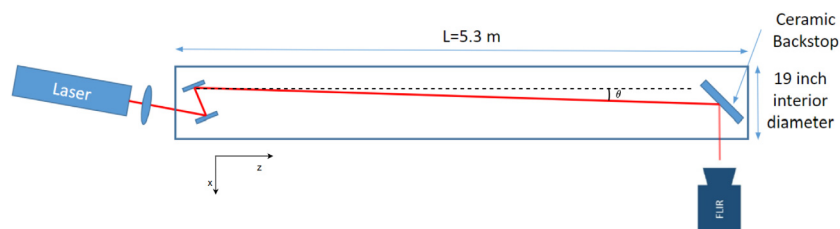


Fig. 2. Top-down view of the chamber.

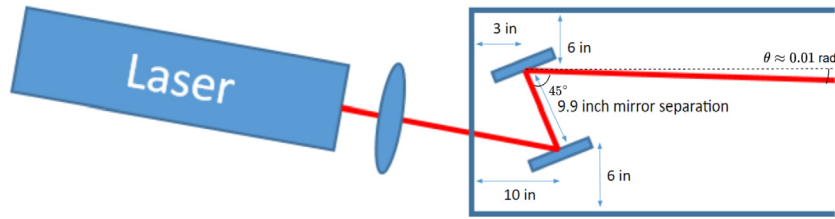


Fig. 3. Zoomed-in view of the chamber with the tilting angle θ . Since the initial reflections are not simulated, the first incident angle is not specified.

in the transverse plane [13]. This simulation architecture forms the basis of the steady-state simulation developed in Ref. [16], where the steady-state flow is computed along two-dimensional slices across the propagation direction, and the fluid temperature fluctuations are linearly interpolated between transverse slices.

The fluid is assumed to be incompressible and governed by the Boussinesq approximation for buoyancy-driven flows. Since the simulated flow is two-dimensional, we solve the stream function–vorticity form of the nondimensional governing equations [27],

$$(\mathbf{u} \cdot \nabla) T = \frac{1}{\text{Pe}} \nabla^2 T + \text{St} |V|^2, \quad (1a)$$

$$(\mathbf{u} \cdot \nabla) \omega = \frac{1}{\text{Re}} \nabla^2 \omega + \text{Ri} \partial_x T, \quad (1b)$$

$$\nabla^2 \psi = -\omega, \quad (1c)$$

$$u = \partial_y \psi, \quad v = -\partial_x \psi, \quad (1d)$$

with vorticity $\omega = \partial_x v - \partial_y u$, stream function ψ , temperature fluctuation T , flow velocity $\mathbf{u} = (u, v)$, and normalized laser irradiance $|V|^2$. The nondimensional parameters are, respectively, the Peclet (Pe), Reynolds (Re), Richardson (Ri), and Stanton (St) numbers that are defined as follows:

$$\text{Re} = \frac{L_x}{\nu}, \quad \text{Pe} = \frac{L_x}{\mu}, \quad \text{Ri} = g L_x, \quad \text{St} = \frac{\beta V_0^2 L_x}{\tau_0}. \quad (2)$$

There is an implicit assumption of a characteristic velocity $U = 1$ cm/s for each of the nondimensional parameters, which can be set arbitrarily without impacting the flow. The parameters to match the experiment are the length scale $L_x = 0.225$ cm as the beam radius, the acceleration due to gravity $g = 981$ cm/s², the kinematic viscosity $\nu = 0.15$ cm²/s, the thermal diffusivity $\mu = 0.2$ cm²/s, the temperature scale $\tau_0 = 296$ K, the laser–fluid absorption constant $\beta = 4.02 \frac{\text{cm}^2 \text{K}}{\text{J}}$, and the peak aperture laser intensity V_0^2 , which varies between 18.9 and 68.3 W/cm². The Re, Pe, and Ri numbers take on the values $\text{Re} = 1.5$, $\text{Pe} = 1.125$, and $\text{Ri} = 220.7$. The Stanton number can be thought of as a measure of the heat deposition from the laser into the flow, and thus depends on the product of the laser irradiance with the laser–fluid absorption constant β . This parameter is related to the more common extinction coefficient α via $\beta = \frac{\alpha}{\rho c_p}$, where $\alpha = 0.48$ m⁻¹ is the estimate for the extinction coefficient which is the laser wavelength within the

Table 1. Fixed Parameters

Parameter	Description	Value	Units
λ	Wavelength	1944.867	nm
k	Wavenumber	$3.23065 \cdot 10^4$	cm ⁻¹
L_x	Beam radius/length scale	2.25	mm
τ_0	Ambient temperature	296	K
ν	Kinematic viscosity	0.15	cm ² /s
B5	Thermal diffusivity	0.2	cm ² /s
g	Gravitational acceleration	981	cm/s ²
β	Laser–fluid absorption constant	4.02	$\frac{\text{cm}^2 \text{K}}{\text{J}}$
α	Extinction coefficient	0.48	m ⁻¹
n_0	Ambient refractive index	1.0003	–
D	Domain width	42	cm
θ	Beam tilt angle	0.01	rad
x_0	Initial beam location	–8.9	cm
Re	Reynolds number	1.5	–
Pe	Peclet number	1.125	–
Ri	Richardson number	220.7	–

water absorption band, obtained from the previous experiments with the same chamber [23].

The beam amplitude V is evolved according to the paraxial equation in nondimensional units [28],

$$\frac{\partial V}{\partial z} = \left(\frac{i}{2n_0 F} \nabla_{\perp}^2 - i L_z n_1 k - \frac{L_z}{2} \alpha \right) V, \quad (3)$$

where $F = \frac{L_x^2 k}{L_z}$ is the Fresnel number [2,3], L_z is the propagation distance of either 3 or 5 m, ∇_{\perp}^2 is the Laplacian in the transverse (x,y) plane, $k = \frac{2\pi}{\lambda} = 3.23065 \times 10^4$ cm⁻¹ is the laser wavenumber, $n_0 = 1.0003$ is the ambient refractive index for air, and α is the same extinction coefficient defined above. The refractive index fluctuation n_1 is linearly related to the spatially varying fluid temperature fluctuations according to $n_1(x, y, z) = (1 - n_0) T(x, y, z)$ [29]. The coupling of the beam response to the fluid is thus contained in this fluctuation. The normalized and nondimensional beam amplitude V_0 at the beginning of propagation takes the form of a Gaussian with a Zernike tilt aberration [30] such that

$$V_0(x, y) = e^{i L_x k \theta x} e^{-\left(\left(x - \frac{x_0}{L_x} \right)^2 + y^2 \right)}. \quad (4)$$

Tables 1 and 2 summarize each of the parameter values for the experiments and simulation.

Table 2. Variable Parameters

Power	V_0^2	St	Propagation Distance	Fr
1.5 W	18.9 W/cm ²	0.0541	3 m	5.45
2.5 W	31.4 W/cm ²	0.0901	5 m	3.27
3.5 W	44.0 W/cm ²	0.1262		
4.5 W	56.6 W/cm ²	0.1622		
5.43 W	68.3 W/cm ²	0.1958		

B. Solution Methods

To solve for the steady-flow solutions to the Boussinesq equations (1), a Padé–Newton procedure is used [22]. The method presented in Ref. [22] is extended to allow for irregular domains, using radial basis functions to approximate differential operators [14,31,32]. The flow is assumed to be two-dimensional along a transverse slice of the propagation chamber at the longitudinal location z_j .

Spatial derivatives in the direction transverse to the beam propagation were approximated using radial basis function-generated finite differences (RBF-FDs) [33–38]. RBF-FD methods are capable of efficiently handling problems that benefit from nonuniform discretizations. In particular, they are useful when attempting to resolve rapidly changing features in the solution to a PDE [31]. A description of their implementation is provided in Appendix A, where the RBF interpolants used here utilize the polyharmonic spline RBF $\phi(r) = r^7$ and supplemental bivariate polynomials up to degree $m = 7$. Figure 4 illustrates the 2D computational fluid domain with circular geometry.

The stream function and vorticity are enforced to be zero on the boundary, corresponding to a Navier-slip boundary condition, where the normal component of velocity at the boundary vanishes but the tangential component is not necessarily zero. We also enforce a zero boundary condition for the temperature fluctuation, which assumes perfect conduction of heat out of the chamber. Along the first fluid slice at $z = 0$, we directly apply the Padé–Newton method by first expanding the flow variables in a perturbation series in the St number,

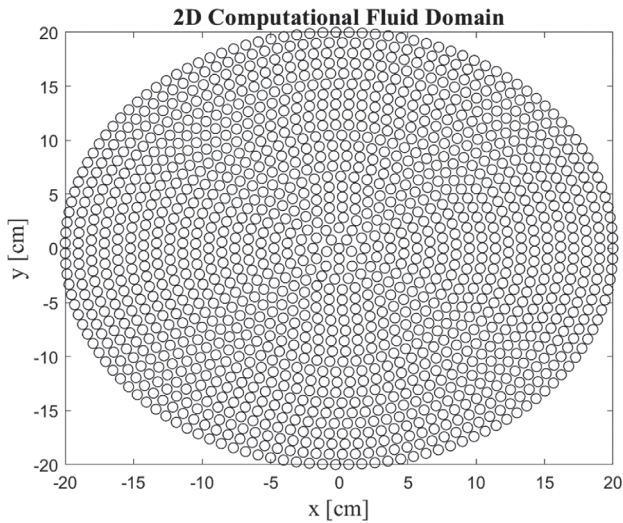


Fig. 4. Illustration of the computational fluid domain with meshless nodes used in the RBF-FD method. The maximum node spacing depicted is $h = 1$, but the simulations were carried out with a more refined $h = 0.125$.

$$T = \sum_{n=0}^{\infty} St^n T_n, \quad \omega = \sum_{n=0}^{\infty} St^n \omega_n, \quad \psi = \sum_{n=0}^{\infty} St^n \psi_n, \quad (5)$$

where each term in the series is computed via the numerical solution to a linear Poisson equation using an RBF-FD discretization. This series representation is analytic only for small values of the St number, so we compute a functional Padé approximant in each flow variable of the form:

$$r^{[n/2k]}(x, y; \varepsilon) = \frac{p(x, y; St)}{q(St)}. \quad (6)$$

The numerator $p(x, y; St)$ and denominator $q(St)$ polynomials are functions of the series terms for each respective flow variable. The spatial dependence in (x, y) is contained only in the numerator polynomial, while the denominator polynomial is strictly a scalar function of St.

In our experiments, the St number is large enough that the functional Padé approximant on its own fails to represent the steady flow to a sufficient degree of accuracy. We thus use the functional Padé approximant as an initialization for a Newton iteration of the form:

$$\mathbf{X}_{n+1} = \mathbf{X}_n - J(\mathcal{F}(\mathbf{X}_n))^{-1} \mathcal{F}(\mathbf{X}_n), \quad (7)$$

where $\mathbf{X}_n = (T_n, \omega_n, \psi_n)$, $\mathcal{F}(\mathbf{X}_n)$ contains the roots of the steady-flow equations (1) with the initial laser intensity, and J denotes the Jacobian of \mathcal{F} at \mathbf{X}_n .

To evolve the beam amplitude V via the Paraxial equation, we linearly interpolate the temperature fluctuations within the volumetric space between the two fluid slices. A Fourier split-step scheme is used to evolve the numerical solution between slices in z .

Given a known steady flow and beam amplitude at the slice z_j , the computation of the fluid slice at the z_{j+1} position requires an iteration in the temperature fluctuation and beam amplitude. Letting T^k and V^k be the temperature and laser amplitude at the k th fluid slice, a sequence of guesses for the temperature $\{\mathcal{T}_n\}$ and the amplitude $\{\mathcal{V}_n\}$ is produced at the next $(k + 1)$ th slice with an initialization,

$$\mathcal{T}_0 = T^k, \quad \mathcal{V}_0 = V^k. \quad (8)$$

These iterative variables are then evolved by implementing the paraxial and fluid solvers, where $T^*(\mathcal{V})$ is the steady temperature fluctuation obtained from the fluid equations for an irradiance $|\mathcal{V}|^2$, and $V^*(\mathcal{T}_i, \mathcal{T}_j)$ is the numerical solution to the paraxial equation between two slices with temperature fluctuations \mathcal{T}_i and \mathcal{T}_j , respectively. The iteration is defined by

$$\mathcal{V}_{n+1} = V^*(T^k, \mathcal{T}_n), \quad (9a)$$

$$\mathcal{T}_{n+1} = T^*(\mathcal{V}_{n+1}). \quad (9b)$$

The initialization for the Newton iteration in computing the step $T^*(\mathcal{V}_{n+1})$ is the previous flow solution $T^*(\mathcal{V}_n)$. If any fluid computational step fails to converge, we apply numerical continuation in St for the same normalized amplitude \mathcal{V} . Convergence is achieved when the fluid response and laser amplitude changes are less than a prescribed threshold, i.e.,

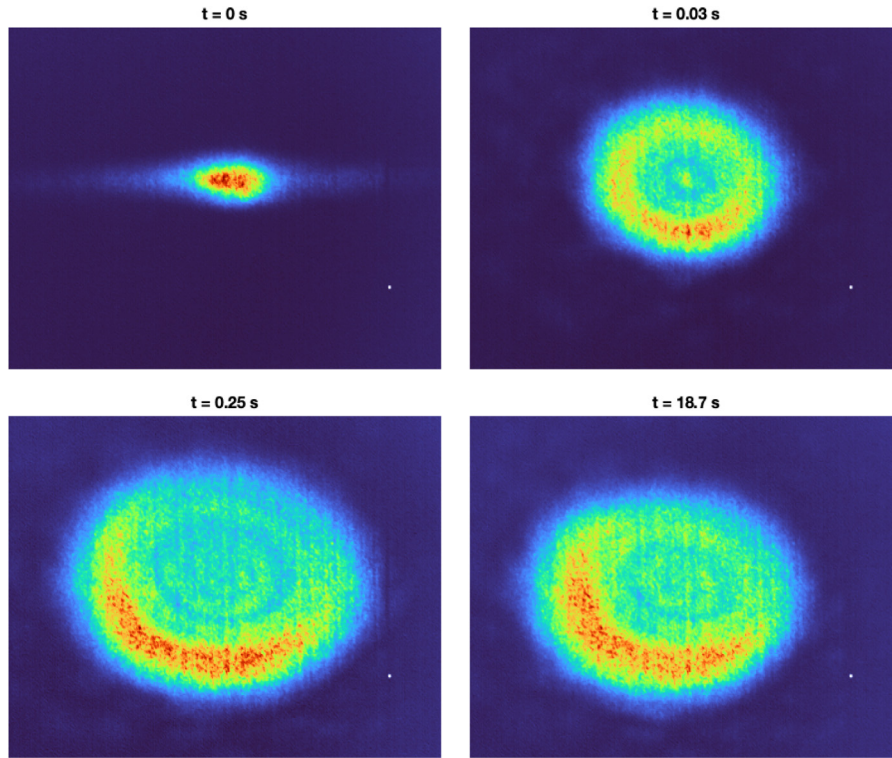


Fig. 5. Time evolution of the thermally bloomed beam within the experimental chamber is depicted. Top left: The beam spot at $t = 0$ displays no visible blooming. Top right: the beam profile at $t = 0.03$ s by which time most of the dynamics have occurred. Bottom left: the beam profile at $t = 0.25$ s as the beam response approaches steady state. Bottom right: the averaged beam profile at $t = 18.7$ s as the final imaging frame is essentially unchanging.

$$\| \mathcal{T}_N - \mathcal{T}_{N-1} \| < \delta_T, \quad \| \mathcal{V}_N - \mathcal{V}_{N-1} \| < \delta_V \quad (10)$$

for $\delta_T = \delta_V = 10^{-15}$. After convergence, the fluid temperature and laser amplitude at the $(k + 1)$ th slice are then updated as

$$T^{k+1} = \mathcal{T}_N, \quad V^{k+1} = \mathcal{V}_N. \quad (11)$$

4. RESULTS

We apply the simulation outlined above to compare each of the propagation distances and beam powers performed in the experiment. The experimental results are captured in a time-dynamic image of intensity over a square window of approximately 12 cm wide. The imaging is performed over a time window of 19.6 s, with a dead time of approximately 1 s before the laser is turned on at $t = 0$ s. The most significant time dynamics occur over a short time span of approximately 0.05 s, with the beam approaching an observable steady-state intensity profile from near 0.25 s to the end of the imaging period at 18.7 s. Figure 5 depicts the time evolution of the experimental beam for propagation over 5 m at 5.43 W. The image plane is oriented such that the resultant crescent is biased away from the direction of the beam tilt and in the direction of the wall closest to the beam spot, as diagrammed in Figs. 2 and 3.

Since our simulation ignores optical aberrations such as turbulence, speckle, or jitter, we average the experimental intensity over the final 10 s of image capture. This approach provides a better basis of comparison for the predicted mathematical steady-state as any time dynamic fluctuations will be smoothed

out. This averaging is performed for each experimental image depicted in Figs. 6 and 7.

In the simulation, the discretization of the fluid and the laser is treated differently due to considerations of computational cost and required resolution to resolve the frequency components arising from the beam tilt. Thus, the 2D fluid equations are solved through a discretization at one resolution, $h_f = 0.125$, while the beam is evolved in the solver for the paraxial equation between slices at a finer resolution $h_L = 0.0039$. This requires a transverse interpolation of the temperature fluctuation over the location of the beam wavefront on top of the volumetric interpolation between 2D slices, spaced according to $\Delta z = 1$ cm. Applying this approach allows for the simultaneous computation of the steady flow over the full experimental domain with the highly resolved beam wavefront over a much smaller subdomain. Solutions were computed on a workstation with 12 Intel Xeon processors, each running at 3.30 GHz, and 96 GB of memory running MATLAB R2023b. The simulations ran for approximately four days for each beam power compared in Figs. 6 and 7.

Figures 6 and 7 provide a direct comparison between the steady-state experimental and simulated intensity after 3 and 5 m of propagation, respectively, for each of the average laser powers. The irradiance spot is shown within a 6 cm \times 6 cm window for both the experiment and the simulation with the same image orientation as Fig. 5. Figure 8 shows a plot of the irradiance along a vertical centerline for the simulated and experimental beams.

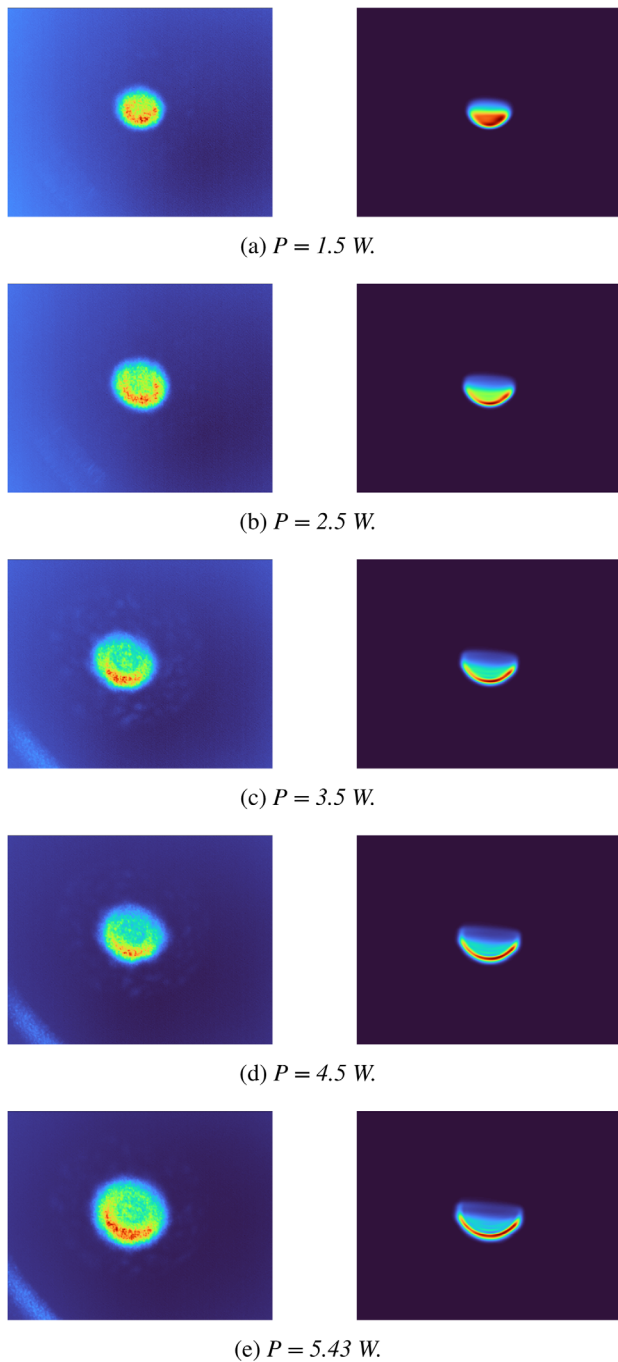


Fig. 6. Comparison between the experiment (left) and the simulation (right) after 3 m of propagation.

The general shape and size of the beam spots agree well between the experiment and the simulation. The width of the bloomed irradiance pattern increases with an increase in beam power to approximately 3.5 cm for the 5.43 W beam. Both display noticeable asymmetry in the intensity distribution in the horizontal direction. This is an addition to the vertical deflection of the beam spot due to convection that is well documented in the thermal blooming literature [20,39,40]. Since our simulations directly solve for the fluid response to the laser heating within the full experimental chamber, this diagonal deflection of the beam intensity is due to corresponding asymmetries in

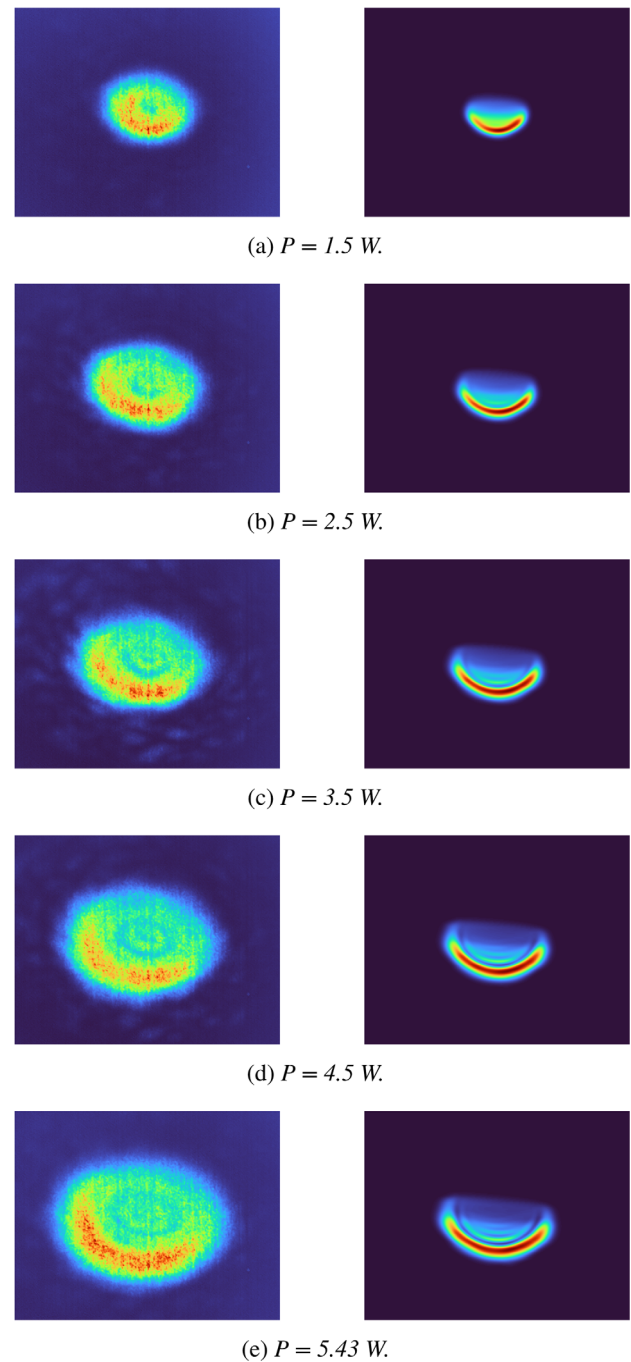


Fig. 7. Comparison between the experiment (left) and the simulation (right) after 5 m of propagation.

the temperature fluctuation about the local wavefront within the propagation chamber. With an increasing beam power, the crescent in the irradiance pattern becomes more pronounced, especially for the simulations. This is explained by the coupling between the temperature fluctuations and the beam evolution as determined by the paraxial equation (3). The temperature fluctuations surrounding the beam increase with an increasing beam power, and therefore the fluctuations in the index of refraction will also increase—leading to an increased deflection of the beam intensity. Figure 9 depicts the simulated streamlines and temperature fluctuations at $z = 0$ m and $z = 5$ m for

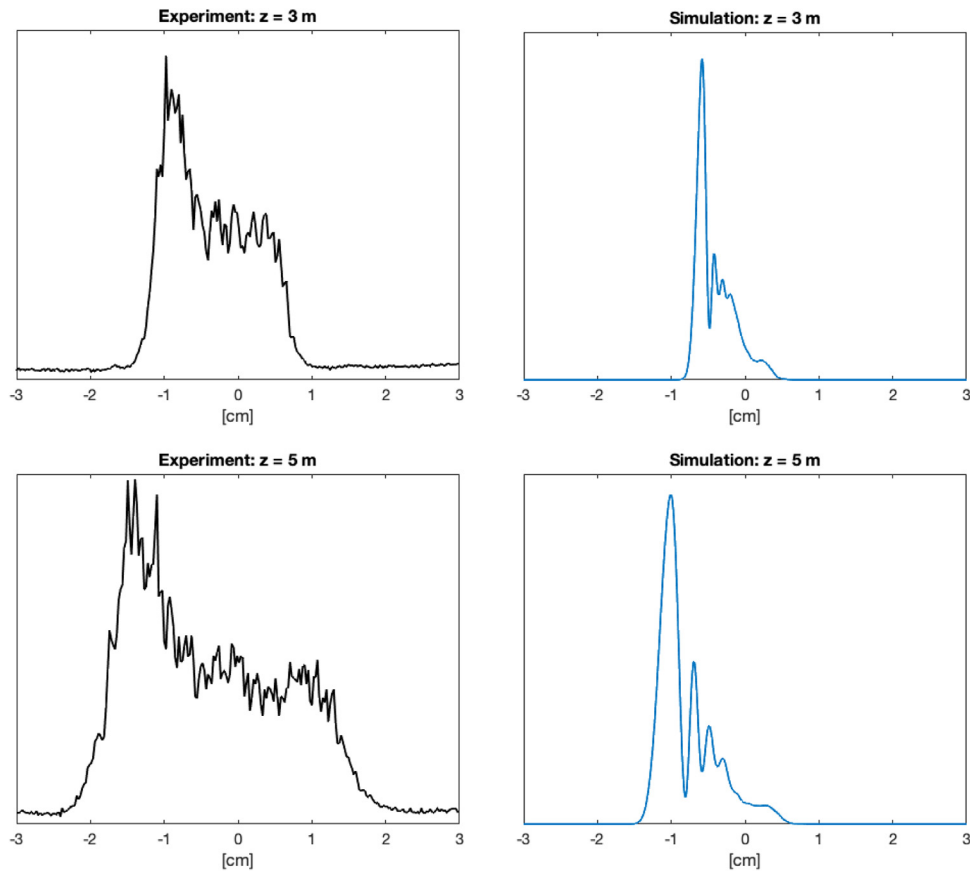


Fig. 8. Irradiance profiles of the simulated and experimental beam at $P = 5.43$ W along a vertical centerline. The vertical axis measures the normalized irradiance, which is plotted against the vertical deviation in the y -coordinate direction. Overall, the deflection of irradiance is well captured in the simulations, but the experimental profiles are wider and have less pronounced annular distortions within the beam.

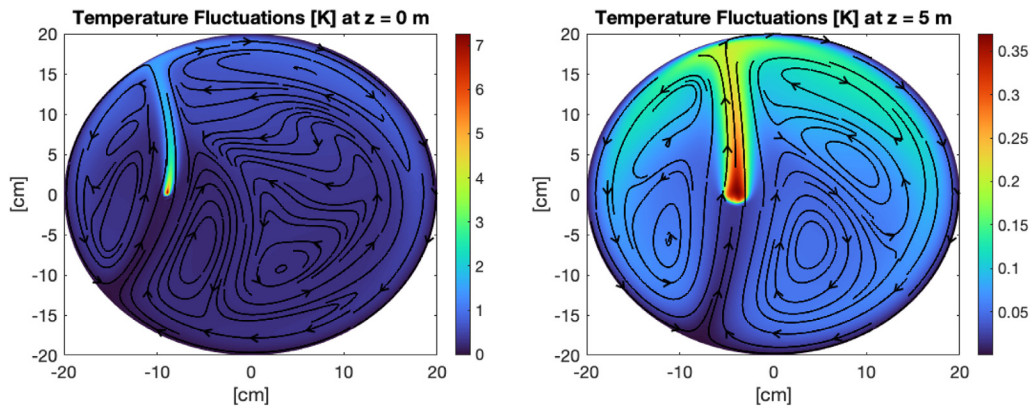


Fig. 9. Temperature fluctuation in degrees K and the streamlines in the fluid at $z = 0$ m and $z = 5$ m are provided, respectively. The fluid experiences the most heating at the beginning of the propagation before the beam loses energy due to absorption. The asymmetric distribution of the temperature fluctuation about the local beam spot is the mechanism for the deflection characteristic of thermal blooming.

$P = 5.43$ W, and Figs. 10 and 11 plot the steady fluid velocity and temperature fluctuation profiles along the $y = 0$ centerline for the same power and distances. Figure 12 provides the peak irradiance and total power of the simulated beam as a function of propagation distance.

The majority of heat deposition into the fluid occurs at the beginning of propagation within the chamber. The beam quickly loses intensity as it propagates over the length of the

chamber, and thus the temperature fluctuation decreases as a function of z over the transverse chamber domain. Since the beam is transversely localized in the negative x -direction, the temperature fluctuation induces a flow with a rightward component. The beam intensity will then deflect in the direction of the induced convective flow, which yields the asymmetric crescent in the negative- x direction.

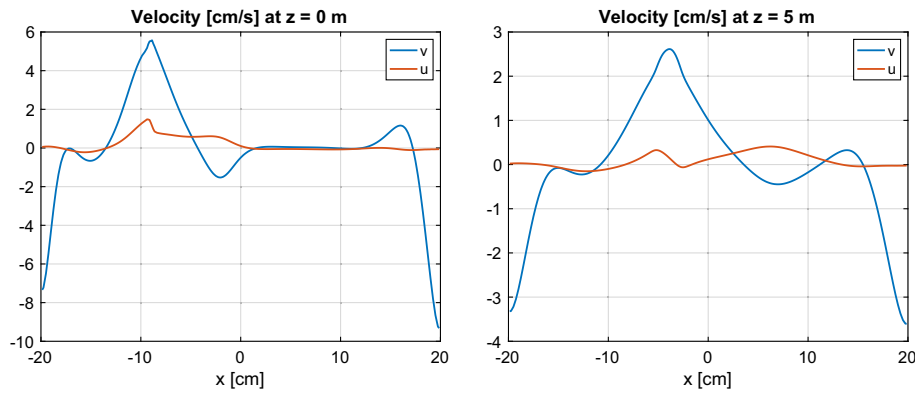


Fig. 10. Steady fluid velocities u and v are plotted as a function of the transverse- x coordinate along the $y = 0$ centerline. At $z = 0$ m and $z = 5$ m, the beam is approximately centered at $x = -8.9$ cm and $x = -4.9$ cm, respectively. Both u and v are positive at the location of the beam spot for each distance, so the local velocity vector points upward and to the right.

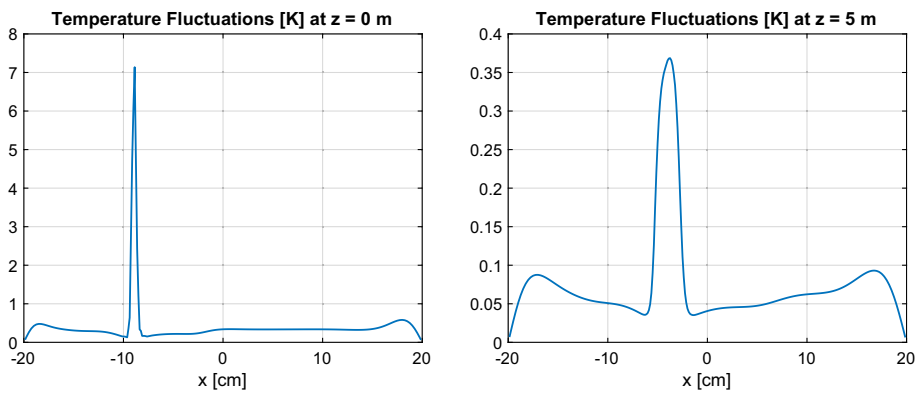


Fig. 11. Steady temperature fluctuation T is plotted as a function of the transverse- x coordinate along the $y = 0$ centerline. The temperature fluctuation increases sharply around the location of beam forcing, resulting in sharp refractive index changes as the beam propagates through.

The departures between the experimental and simulated beam spots can be explained through several factors. The reflections of the beam off of the mirrors at the beginning of the chamber are not simulated, which is where the beam deposits the most energy along its propagation path. There is some uncertainty in the exact value of the absorption coefficient within the chamber, which directly influences the amount of energy deposition and subsequent temperature fluctuations around the beam spot. Further departures can be due to non-ideal Gaussian beam quality in the experiment and some uncertainty in the geometry of the experimental setup. The largest source of disagreement, however, may come from the comparison between a time-averaged experimental beam and a simulated beam in a theoretical steady state. Although the chamber is climate controlled, there are still thermal fluctuations from the outside environment that can result in a less coherent distribution of temperature fluctuations around the beam spot. After performing the time-averaging, many of the irradiance fluctuations become smoothed out in the experimental beam, which has the effect of smoothing out some of the thermal distortions. This can partially explain the differences in the structure of the distortion rings seen between the experiment and the simulation, along with the other factors mentioned above. In future experiments, it would be beneficial to explore ways to reduce thermal fluctuations outside the chamber to achieve a more

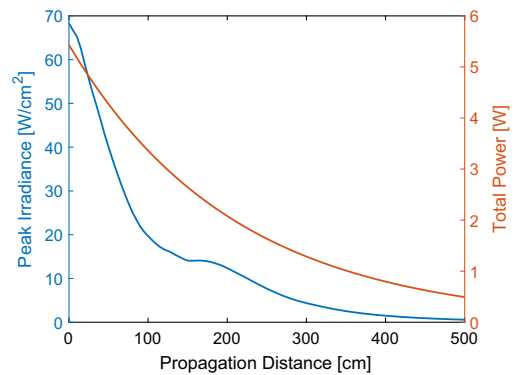


Fig. 12. Peak transverse irradiance (blue) and the total beam power (red) are shown as a function of the propagation distance for the 5.43 W simulated beam. The total power decays exponentially according to the optical extinction coefficient, while the peak irradiance is influenced by spreading, optical losses, and phase distortion.

consistent steady fluid flow. To better match the experimental results, the simulation can be improved by increasing spatial resolution in the beam field and in the quasi-2D steady flow representation, especially in the rapidly changing regions in the temperature field.

5. CONCLUSION

The results of this investigation demonstrate that the flow response to a tilted beam propagating off-center within an experimental enclosure can induce asymmetries in the thermally bloomed beam spot about the vertical axis. These findings were studied experimentally and via simulation with a fully coupled model for laser–fluid interaction. The beam was tuned to a wavelength within a water absorption band with a Stanton number equivalent to a high-power beam through a transmission window. Five different beam powers were investigated, with a good agreement between the experiment and the simulation with respect to the thermally bloomed beam size and crescent shape. The methodology of simulation can be used to predict steady-state irradiance patterns for future experiments in thermal blooming. Future work should examine thermal blooming through a chamber filled with aerosols and the thermal blooming of multiple beams combining at a target within a finite chamber.

APPENDIX A

The following is a description of the RBF-FD method utilized to discretize the steady fluid equations. Consider the disk of diameter $\frac{D}{L_x}$ as the computational domain $\Omega \subset \mathbb{R}^2$ in the transverse direction. The components of any \mathbf{x} in the domain are given by $\mathbf{x} = [x \ y]^T$. At each element, \mathbf{x}_k , of a set of discrete node locations, $\mathcal{S}_N = \{\mathbf{x}_k\}_{k=1}^N$, the spatial derivatives in (3.0.1) and (6) are approximated. This is completed by applying the action of the linear differential operators to local interpolants of ψ , ω , T , u , and v over $\mathcal{N}_{k,n} = \{\mathbf{x}_{k,j}\}_{j=1}^n$, which is the set of n points in \mathcal{S}_N nearest to \mathbf{x}_k .

Each local interpolant is a linear combination of (conditionally) positive definite kernels, φ , evaluated at the points in $\mathcal{N}_{k,n}$,

$$\phi_{k,n,j}(\mathbf{x}) := \varphi(\|\mathbf{x} - \mathbf{x}_{k,j}\|_2), \quad j = 1, 2, \dots, n,$$

and bivariate polynomial terms, $\{\pi_{k,l}(\mathbf{x})\}_{l=1}^{M_m}$, up to total degree m , with $M_m = (m+1)(m+2)/2$. For instance, the local interpolant of a sufficiently smooth function $f: \mathbb{R}^2 \mapsto \mathbb{R}$ is constructed as

$$s_{k,n,m}[f](\mathbf{x}) := \sum_{j=1}^n \lambda_{k,n,m,j}[f] \phi_{k,n,j}(\mathbf{x}) + \sum_{l=1}^{M_m} \gamma_{k,n,m,l}[f] \pi_{k,l}(\mathbf{x}).$$

To ensure that $s_{k,n,m}[f]$ interpolates f at the set of points in $\mathcal{N}_{k,n}$, the set of coefficients is chosen to satisfy the interpolation conditions ($j = 1, 2, \dots, n$),

$$s_{k,n,m}[f](\mathbf{x}_{k,j}) = f(\mathbf{x}_{k,j}),$$

and the typical constraints to ensure existence of a unique interpolant ($l = 1, 2, \dots, M_m$) (see, e.g., Ref. [41]),

$$\sum_{j=1}^n \lambda_{k,n,m,j}[f] \pi_{k,l}(\mathbf{x}_{k,j}) = 0.$$

The interpolant can alternatively be formulated through a change of basis as a linear combination of cardinal functions that span the same space. That is,

$$s_{k,n,m}[f](\mathbf{x}) = \sum_{i=1}^n \psi_{k,n,m,i}(\mathbf{x}) f(\mathbf{x}_{k,i}),$$

where the new set of basis functions satisfy the cardinal property,

$$\psi_{k,n,m,i}(\mathbf{x}_{k,j}) = \begin{cases} 1 & i = j \\ 0 & i \neq j \end{cases}.$$

The action of a linear operator \mathcal{L} on f at \mathbf{x}_k is then approximated by

$$(\mathcal{L}f)(\mathbf{x}_k) \approx (\mathcal{L}s_{k,n,m}[f])(\mathbf{x}_k) = \sum_{i=1}^n w_{k,i} f(\mathbf{x}_{k,i})$$

with $w_{k,i} = (\mathcal{L}\psi_{k,n,m,i})(\mathbf{x}_k)$. Detailed discussion of the accuracy of this approximation is given in, for instance, Ref. [31]. The action of \mathcal{L} at all points in \mathcal{S}_N can then be computed simultaneously through the matrix multiplication,

$$D\mathbf{f} \approx [\mathcal{L}f(\mathbf{x})|_{\mathbf{x}=\mathbf{x}_1} \ \mathcal{L}f(\mathbf{x})|_{\mathbf{x}=\mathbf{x}_2} \ \cdots \ \mathcal{L}f(\mathbf{x})|_{\mathbf{x}=\mathbf{x}_N}]^T, \quad (\text{A1})$$

where the k th component of \mathbf{f} is $f(\mathbf{x}_k)$. In this case, D is an $N \times N$ matrix that is sparse as long as the number of nearest neighbors, n , is much less than the total number of points, N . The entries of row k of the matrix operator are defined as

$$[D]_{ki} = \begin{cases} w_{k,i} & \text{if } \mathbf{x}_{k,i} = \mathbf{x}_i \text{ for some } (k, i) \\ 0 & \text{otherwise.} \end{cases}$$

Funding. Air Force Office of Scientific Research; Joint Directed Energy Transition Office.

Acknowledgment. This report was prepared as an account of work sponsored by an agency of the U.S. Government. Neither the U.S. Government nor any agency thereof, nor any of their employees, make any warranty, express or implied, or assumes any legal liability or responsibility for the accuracy, completeness, or usefulness of any information, apparatus, product, or process disclosed, or represents that its use would not infringe privately owned rights. Reference herein to any specific commercial product, process, or service by trade name, trademark, manufacturer, or otherwise does not necessarily constitute or imply its endorsement, recommendation, or favoring by the U.S. Government or any agency thereof. The views and opinions of authors expressed herein do not necessarily state or reflect those of the U.S. Government or any agency thereof.

Disclosures. The authors declare no conflicts of interest.

Data availability. Data underlying the results presented in this paper are not publicly available at this time but may be obtained from the authors upon reasonable request.

REFERENCES

1. J. S. Lane, "Steady state thermal blooming with convection: modeling, simulation and analysis," Theses and Dissertations, 7660 (AFIT, 2023), <https://scholar.afit.edu/etd/7660>.
2. F. G. Gebhardt, "High power laser propagation," *Appl. Opt.* **15**, 1479–1493 (1976).
3. D. C. Smith, "High-power laser propagation: thermal blooming," *Proc. IEEE* **65**, 1679–1714 (1977).
4. R. C. Lawrence, A. Nitkowski, C. Higgs, *et al.*, "Thermal-blooming compensation using target-in-the-loop techniques," *Proc. SPIE* **5895**, 58950N (2005).
5. B. Johnson and C. A. Primmerman, "Experimental observation of thermal-blooming phase-compensation instability," *Opt. Lett.* **14**, 639–641 (1989).

6. M. F. Spencer and S. J. Cusumano, "Impact of branch points in adaptive optics compensation of thermal blooming and turbulence," *Proc. SPIE* **8165**, 816503 (2011).
7. Q. Zhang, Q. Hu, H. Wang, *et al.*, "High-precision calculation and experiments on the thermal blooming of high-energy lasers," *Opt. Express* **31**, 25900–25914 (2023).
8. M. J. Schmitt, "Mitigation of thermal blooming and diffraction effects with high-power laser beams," *J. Opt. Soc. Am. B* **20**, 719–724 (2003).
9. Y. Zhang, X. Ji, X. Li, *et al.*, "Thermal blooming effect of laser beams propagating through seawater," *Opt. Express* **25**, 5861–5875 (2017).
10. M. F. Spencer, "Wave-optics investigation of turbulence thermal blooming interaction: II. Using time-dependent simulations," *Opt. Eng.* **59**, 081805 (2020).
11. K. Petrowski, D. Limsui, C. Menyuk, *et al.*, "Turbulent thermal blooming," *Proc. SPIE* **6951**, 33–41 (2008).
12. J. Wallace and J. Pasciak, "Thermal blooming of a rapidly moving laser beam," *Appl. Opt.* **15**, 218–222 (1976).
13. B. F. Akers and J. A. Reeger, "Numerical simulation of thermal blooming with laser-induced convection," *J. Electromagn. Waves Appl.* **33**, 96–106 (2019).
14. B. F. Akers, S. T. Fiorino, and J. A. Reeger, "Thermal blooming with laser-induced convection: radial basis function simulation," *Appl. Opt.* **62**, G77–G84 (2023).
15. J. S. Lane and B. F. Akers, "Two-dimensional steady Boussinesq convection: existence, computation and scaling," *Fluids* **6**, 425 (2021).
16. J. S. Lane, J. Cook, M. Richardson, *et al.*, "Numerical simulation of steady-state thermal blooming with natural convection," *Appl. Opt.* **62**, 2092–2099 (2023).
17. B. Johnson, "Thermal-blooming laboratory experiments," *Linc. Lab. J.* **5**, 151–170 (1992).
18. G. N. Grachev, A. A. Zemlyanov, A. G. Ponomarenko, *et al.*, "Thermal self-action of high-power continuous and pulse-periodic CO₂ laser radiation in air: I. Laboratory experiments," *Atmos. Ocean. Opt.* **27**, 115–122 (2014).
19. B. Hafizi, J. Penano, R. Fischer, *et al.*, "Determination of absorption coefficient based on laser beam thermal blooming in gas-filled tube," *Appl. Opt.* **53**, 5016–5023 (2014).
20. S. Reich, S. Schäffer, M. Lueck, *et al.*, "Continuous wave high-power laser propagation in water is affected by strong thermal lensing and thermal blooming already at short distances," *Sci. Rep.* **11**, 22619 (2021).
21. N. R. V. Zandt, S. T. Fiorino, and K. J. Keefer, "Enhanced, fast-running scaling law model of thermal blooming and turbulence effects on high energy laser propagation," *Opt. Express* **21**, 14789 (2013).
22. J. S. Lane and B. F. Akers, "Steady Boussinesq convection: parametric analyticity and computation," *Stud. Appl. Math.* **10**, e12740 (2024).
23. J. Cook, P. Roumayah, D. J. Shin, *et al.*, "Narrow linewidth 80 W tunable thulium-doped fiber laser," *Opt. Laser Technol.* **146**, 107568 (2022).
24. S. T. Fiorino, R. J. Bartell, M. J. Krizo, *et al.*, "A first principles atmospheric propagation and characterization tool: the laser environmental effects definition and reference (LEEDR)," *Proc. SPIE* **6878**, 68780B (2008).
25. P. Sprangle, J. Penano, and B. Hafizi, "Optimum wavelength and power for efficient laser propagation in various atmospheric environments," *J. Dir. Energy* **2**, 71–95 (2006).
26. M. Lax, W. H. Louisell, and W. B. McKnight, "From Maxwell to paraxial wave optics," *Phys. Rev. A* **11**, 1365 (1975).
27. L. Quartapelle, *Numerical Solution of the Incompressible Navier-Stokes Equations*, 1st ed. (Birkhauser Verlag, 1993).
28. P. Sprangle, J. R. Penano, A. Ting, *et al.*, "Propagation of high-energy lasers in a maritime atmosphere," in *NRL Review* (2004), pp. 59–65.
29. C. Hogge, "Propagation of high-energy laser beam in the atmosphere," Tech. rep. (Air Force Weapons Laboratory, 1974).
30. J. Alda, J. Alonso, and E. Bernabeu, "Characterization of aberrated laser beams," *J. Opt. Soc. Am. A* **14**, 2737–2747 (1997).
31. J. A. Reeger, "Adaptivity in local kernel based methods for approximating the action of linear operators," *SIAM J. Sci. Comput.* **46**, A2683–A2708 (2024).
32. B. Akers, T. Liu, and J. Reeger, "A radial basis function finite difference scheme for the Benjamin-Ono equation," *Mathematics* **9**, 65 (2020).
33. B. Fornberg and N. Flyer, *A Primer on Radial Basis Functions with Applications to the Geosciences* (SIAM, 2015).
34. M. D. Buhmann, "New developments in the theory of radial basis function interpolation," in *Multivariate Approximation: From CAGD to Wavelets* (World Scientific, 1993), pp. 35–75.
35. J. A. Reeger, "Approximate integrals over the volume of the ball," *J. Sci. Comput.* **83**, 45 (2020).
36. J. A. Reeger, B. Fornberg, and M. L. Watts, "Numerical quadrature over smooth, closed surfaces," *Proc. R. Soc. Lond. A* **472**, 20160401 (2016).
37. J. A. Reeger and B. Fornberg, "Numerical quadrature over the surface of a sphere," *Stud. Appl. Math.* **137**, 174–188 (2016).
38. J. A. Reeger and B. Fornberg, "Numerical quadrature over smooth surfaces with boundaries," *J. Comput. Phys.* **355**, 176–190 (2018).
39. L. Lu, Z. Wang, P. Zhang, *et al.*, "Thermal blooming induced phase change and its compensation of a Gaussian beam propagation in an absorbing medium," *Opt. Lett.* **46**, 4304–4307 (2021).
40. R. T. Brown and D. C. Smith, "Aerosol-induced thermal blooming," *J. Appl. Phys.* **46**, 402–405 (1975).
41. H. Wendland, *Scattered Data Approximation* (Cambridge University, 2005), Vol. **17**.